Journal of Computational Applied Mechanics 2026, 57(4): 731-751

DOI: 10.22059/jcamech.2026.424526.1983

RESEARCH PAPER

Reduced-Order Learning of Cerebral Aneurysm Hemodynamics: Comparing POD, PCA, and Autoencoder Models Coupled with TCN

M. Barzegar Gerdroodbary [a,b *] , Seyedeh Zahra Sajadi [c]

[a] *Department of Electromechanical Engineering, C-MAST-Center for Mechanical and Aerospace Science and Technology, Universidade da Beira Interior, Covilha, Portugal*

[b] *Department of Mechanical Engineering, Iranian Research Organization for Science and Technology (IROST), Tehran, Iran*

[c] *Department of Computer Science, University of Mazandaran, Iran*

Abstract

Accurate characterization of cerebral aneurysm hemodynamics is important for understanding flow-related mechanisms associated with aneurysm progression and for quantifying the hemodynamic modifications induced by endovascular treatment. However, high-fidelity transient computational fluid dynamics (CFD) simulations are computationally demanding, particularly when time-resolved three-dimensional hemodynamic fields are required. This study presents a comparative evaluation of three reduced-order modeling (ROM) strategies—proper orthogonal decomposition (POD), principal component analysis (PCA), and Autoencoder—coupled with a temporal convolutional network (TCN) for reconstruction and temporal prediction of hemodynamics in a patient-specific internal carotid artery saccular aneurysm before and after endovascular coiling. Pulsatile, non-Newtonian blood flow was simulated using the Casson model, while the coiled aneurysm region was represented through a porous-medium formulation. Wall shear stress (WSS/AWSS), oscillatory shear index (OSI), and pressure fields were extracted from CFD simulations and compressed into low-dimensional representations using the three ROM approaches. A common TCN architecture was subsequently employed to learn the temporal evolution of the reduced coefficients and predict future hemodynamic states. The results demonstrate that coiling substantially suppresses intra-aneurysmal flow activity and modifies the spatial distributions of WSS, OSI, and pressure. The modal analysis further shows that approximately 99% of the dominant information can be retained using a relatively small number of modes or latent variables, although the required dimensionality varies among hemodynamic quantities and ROM techniques. All three hybrid frameworks successfully reconstructed the major spatial characteristics of the CFD fields, while prediction accuracy decreased with increasing forecast horizon. Among the investigated approaches, PCA–TCN showed the most stable predictive behavior for the present dataset and effectively reproduced the principal distributions of WSS, OSI, and pressure in both original and coiled configurations. These findings demonstrate the potential of ROM–TCN frameworks as computationally efficient surrogate models for time-resolved assessment of cerebral aneurysm hemodynamics and treatment-induced flow alterations.

Keywords: : Cerebral saccular aneurysm; Endovascular coiling; Computational fluid dynamics (CFD); Reduced-order modeling (ROM); Machine learning;

1. Introduction

Cerebral aneurysms are localized pathological dilations of intracranial arteries that arise from progressive weakening and remodeling of the vascular wall under the combined influence of biological processes, vascular morphology, and repetitive hemodynamic loading [1, 2]. They frequently develop at arterial bifurcations and highly curved vascular segments, where complex flow patterns and nonuniform mechanical stresses are present [3, 4]. Among the different aneurysm morphologies, saccular intracranial aneurysms are of particular clinical importance because of their prevalence and potential for rupture. These aneurysms are characterized by a pouch-like sac connected to the parent vessel through a neck, creating a flow environment markedly different from that of the surrounding artery [5]. Blood entering the sac can generate a concentrated inflow jet, wall impingement, recirculation zones, flow separation, and spatially heterogeneous shear stresses. Progressive alterations in the aneurysm wall may eventually result in rupture and subarachnoid hemorrhage, which is associated with substantial mortality and neurological morbidity. Understanding the interaction between aneurysm morphology, treatment, and local hemodynamics is therefore important for investigating aneurysm progression and the mechanisms associated with rupture [6, 7].

Reliable identification and characterization of cerebral aneurysms are essential for assessing their condition and supporting treatment planning. Conventional clinical evaluation is primarily based on medical imaging, aneurysm size and morphology, anatomical location, growth history, and patient-specific factors [8, 9]. However, geometrically similar aneurysms may exhibit substantially different blood-flow characteristics, motivating the use of patient-specific hemodynamic analysis as a complementary biomechanical tool. Computational fluid dynamics (CFD) provides detailed spatial and temporal information on aneurysmal blood flow and enables evaluation of quantities such as wall shear stress (WSS), oscillatory shear index (OSI), and pressure throughout the cardiac cycle. WSS characterizes the tangential force imposed by blood flow on the vessel wall, whereas OSI describes temporal changes in the direction of the shear stress and can identify regions exposed to strongly oscillatory flow [10, 11, and 12]. Pressure represents another component of the mechanical loading acting on the aneurysmal wall. Importantly, these quantities should not be considered individually as deterministic indicators of rupture; rather, their spatial and temporal distributions provide complementary information about the local biomechanical environment [13]. CFD is also particularly useful for investigating endovascular coiling, because comparison of the same aneurysm before and after treatment can reveal how coil-induced obstruction modifies intra-aneurysmal circulation, suppresses the inflow jet and recirculation, and redistributes important hemodynamic quantities [14, 15, and 16]. In fig. 1, schematic of the blood flow inside the sac with/without coiling are demonstrated.

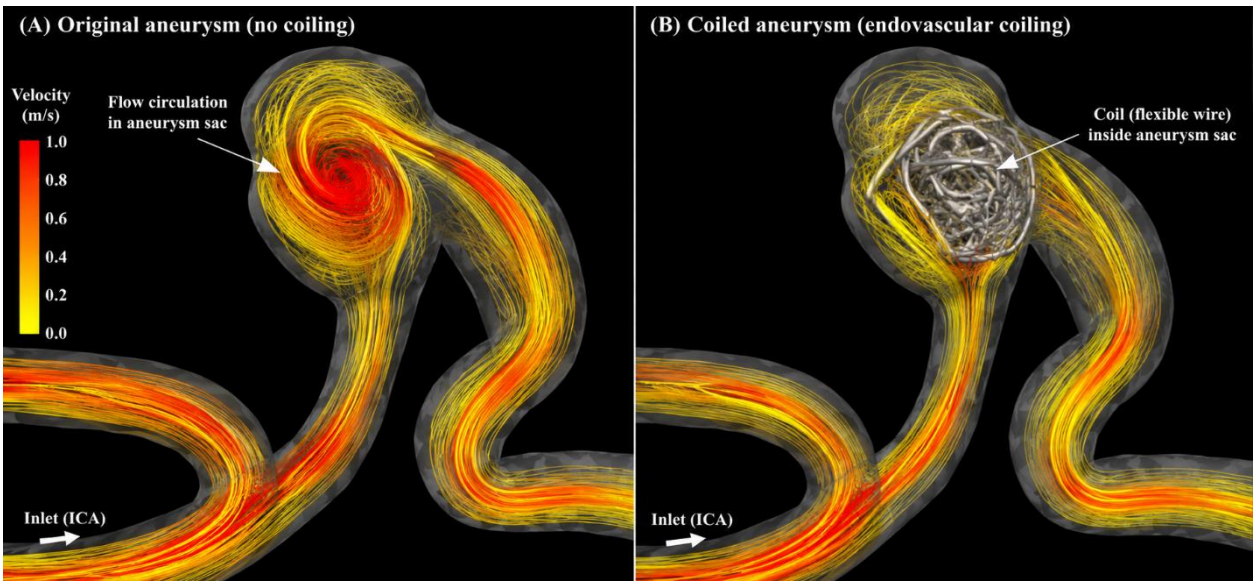

Fig 1: Schematic of the blood flow in the sac region in original patient with/without endovascular coiling

Although CFD offers high-resolution characterization of these changes, transient patient-specific simulations can be computationally expensive because they require complex vascular geometries, sufficiently refined meshes, small time steps, and simulations over multiple cardiac cycles [17, 18]. Furthermore, storing and processing the resulting three-dimensional transient fields generates high-dimensional datasets that complicate repeated analyses and rapid

prediction. This challenge has encouraged the development of hybrid reduced-order modeling and machine-learning frameworks in which high-fidelity CFD data are first compressed into a low-dimensional representation and subsequently predicted using a temporal learning algorithm. Reduced-order models (ROMs) can retain the dominant features of the original CFD fields while substantially decreasing the number of variables required to represent the flow [19, 20, and 21]. Temporal predictors such as long short-term memory (LSTM) networks and Temporal Convolutional Networks (TCNs) can then learn the evolution of the reduced variables and forecast unseen portions of the cardiac cycle. TCNs are particularly attractive for transient hemodynamic applications because causal and dilated convolutions can capture temporal dependencies over relatively long sequences while allowing efficient and parallelizable training. Such ROM–TCN frameworks could provide computationally efficient surrogate models for reconstructing and predicting WSS, OSI, pressure, and other flow quantities in both untreated and treated aneurysm configurations.

The effectiveness of a hybrid ROM–TCN framework nevertheless depends strongly on the dimensionality-reduction method used to represent the original CFD fields. Proper Orthogonal Decomposition (POD) represents the flow using a limited number of orthogonal modes selected according to their contribution to the snapshot energy, providing a physically interpretable low-dimensional approximation of complex flow structures. Principal Component Analysis (PCA) similarly projects high-dimensional data onto orthogonal components that capture the dominant variance of the dataset and provides an efficient linear compression strategy. Although POD and PCA are closely related linear projection techniques in many snapshot-based formulations, their implementation and interpretation within data-driven workflows can differ. In contrast, an Autoencoder (AE) uses nonlinear encoder and decoder networks to map the original CFD fields into a compact latent space and reconstruct them, potentially representing nonlinear hemodynamic structures that require a larger number of linear modes [22, 23, and 24]. A direct comparison under identical CFD data, training/testing partitions, and predictive-network settings is therefore needed to determine how the selected ROM influences reconstruction and temporal prediction.

Accordingly, the present study develops a unified framework to compare POD–TCN, PCA–TCN, and Autoencoder–TCN for the reconstruction and prediction of patient-specific cerebral aneurysm hemodynamics. Rather than considering independent aneurysm geometries, the analysis focuses on the same saccular aneurysm in its original untreated state and after endovascular coiling, thereby allowing changes in model performance to be examined alongside treatment-induced alterations in the underlying flow environment. High-fidelity transient CFD data are generated for both configurations, and WSS, OSI, and pressure fields are used to construct and evaluate the three reduced-order representations. Each reduced representation is subsequently coupled with the same TCN-based temporal prediction strategy and assessed over the cardiac cycle using consistent reconstruction and prediction metrics. This design provides a controlled comparison of linear modal reduction and nonlinear latent-space compression while simultaneously examining whether their predictive performance is maintained after the substantial modification of intra-aneurysmal flow produced by coiling. The study therefore aims to identify the strengths and limitations of POD, PCA, and Autoencoder representations for efficient surrogate modeling of pre- and post-coiling cerebral aneurysm hemodynamics, rather than using the predicted hemodynamic quantities themselves as direct clinical indicators of rupture or treatment success.

2. Computational Modeling of Blood Flow in a Patient-Specific Cerebral Aneurysm

2.1. Patient

A patient-specific intracranial aneurysm geometry was selected from the Aneurisk Web Project [25] to investigate cerebral hemodynamics before and after endovascular coiling. The selected geometry corresponds to Patient ID 06, representing an unruptured lateral (LAT) saccular aneurysm located in the internal carotid artery (ICA). The patient was a 45-year-old female with no reported multiple aneurysms. As illustrated in Fig. 2, the reconstructed vascular domain includes the aneurysm sac, parent ICA, and downstream branches, allowing the complex curvature and topology of the patient-specific cerebral vasculature to be retained in the computational model. The untreated configuration is hereafter referred to as the original model, whereas the corresponding geometry incorporating the endovascular treatment is denoted as the coiled model. Using the same vascular geometry for both configurations provides a controlled basis for identifying treatment-induced changes in WSS, OSI, and pressure and for evaluating the performance of the PCA–TCN, POD–TCN, and Autoencoder–TCN reduced-order frameworks.

Ostium (neck) area	34.92 mm²

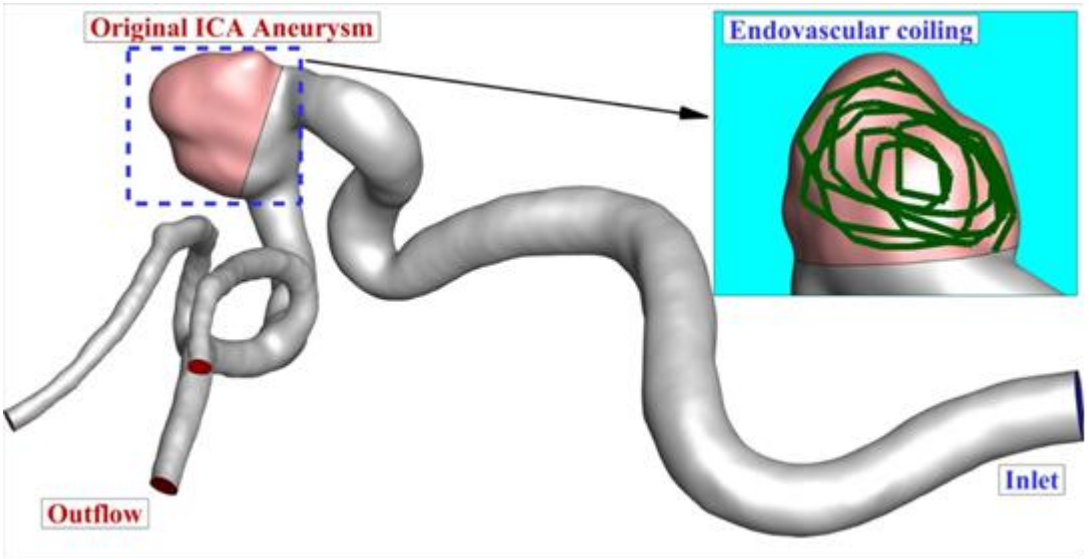

Fig. 2: Patient-specific geometry used for the computational analysis.

The selected aneurysm has a sac volume of 166.77 mm³, surface area of 130.67 mm², and sac section area of 36.61 mm². Its ellipsoidal maximum, intermediate, and minimum semi-axes are 3.839, 2.518, and 2.358 mm, respectively, while the sac centerline length is 5.981 mm. The ostium has an area of 34.924 mm² and perimeter of 22.049 mm, with minimum and maximum dimensions of 2.584 and 4.433 mm, respectively. The calculated aspect ratio and size ratio are 0.944 and 2.129. The parent vessel has a mean radius of 1.702 mm and a length of 88.036 mm, while the sac–neck vessel angle and sac–vessel angle are 31.41° and 45.34°, respectively. These morphological characteristics provide the geometric basis for the patient-specific CFD simulations and subsequent reduced-order analyses. The principal morphological characteristics of the selected patient-specific aneurysm are summarized in Table 1. The selected parameters characterize the overall aneurysm size, neck geometry, and sac–parent-vessel relationship, which are particularly relevant to the development of the intra-aneurysmal flow pattern and the resulting hemodynamic environment.

Table 1: Principal geometrical characteristics of the selected ICA saccular aneurysm (Patient ID 06).

Geometrical feature	Value
Sac volume	166.77 mm³
Sac surface area	130.67 mm²
Ostium (neck) area	34.92 mm²
Aspect ratio	0.944
Size ratio	2.129

The porous region was assigned a porosity of 0.791 and a permeability of 1.2555×10^{-7} m^2. The corresponding viscous resistance was 7.964902×10^{6} m^{-2}, which is the inverse of the specified permeability,

$$\alpha^{-1} = \frac{1}{K}, \tag{1}$$

where K denotes permeability. Accordingly,

$$\frac{1}{1.2555 \times 10^{-7}} \approx 7.9649 \times 10^{6}\ \mathrm{m}^{-2}. \tag{2}$$

The momentum loss introduced by the coil-packed porous region can be represented through a Darcy-type momentum sink,

$$\mathbf{S}_p = -\frac{\mu}{K}\mathbf{u}, \tag{3}$$

whereμ is the local dynamic viscosity and $\mathbf{u}$ is the velocity vector. This resistance suppresses intra-aneurysmal flow and modifies the spatial distribution and temporal evolution of the hemodynamic quantities investigated in this study. The porous-medium approximation therefore provides a computationally tractable representation of the bulk hydraulic influence of coil packing; it is not intended to reproduce the detailed flow around individual coil wires

2.2. CFD Modeling of Patient-Specific Blood Flow

Transient three-dimensional CFD simulations were performed for both the original and coiled aneurysm configurations. Blood was considered an incompressible, non-Newtonian fluid, and the flow was assumed to remain laminar throughout the investigated cardiac cycle [26, 27, and 28]. Because the objective of the present study was to compare the hemodynamic fields and reduced-order prediction performance before and after coiling rather than investigate wall deformation, a non-FSI approach was adopted. Consequently, the vascular walls were assumed rigid with a no-slip boundary condition. The governing equations consist of conservation of mass and momentum,

$$\nabla \cdot \mathbf{u} = 0, \tag{4}$$

And

$$\rho\left[\frac{\partial \mathbf{u}}{\partial t} + (\mathbf{u} \cdot \nabla)\mathbf{u}\right] = -\nabla p + \nabla \cdot [\mu_{\text{eff}}(\nabla \mathbf{u} + \nabla \mathbf{u}^T)], \tag{5}$$

where ρ is blood density, u is the velocity vector, p denotes pressure, μ_{eff} is the apparent non-Newtonian viscosity.

The non-Newtonian behavior of blood was represented using the Casson rheological model [29, 30]. This model was selected because it accounts for the shear-dependent apparent viscosity and yield-stress behavior of blood, which can become relevant in the low-velocity and recirculating regions commonly encountered inside aneurysmal sacs. The Casson relation may be expressed as

$$\tau = \left(\sqrt{\tau_y} + \sqrt{\mu_c \dot{\gamma}}\right)^2, \tag{6}$$

where τ is the shear stress, τ_y is the Casson yield stress, μ_c is the Casson viscosity coefficient, and $\dot{\gamma}$ denotes the shear rate. Blood density was specified as 1050 kg/ m^3, while the Casson parameters were maintained consistently for the original and coiled configurations so that the observed differences resulted from the treatment model rather than changes in blood properties. ANSYS-Fluent software [31] is used for the modeling of the blood flow inside the vessel and sac region.

2.3. Physiological Boundary Conditions and Transient Simulation

Physiologically pulsatile boundary conditions were imposed to reproduce the temporal variation of cerebral blood flow over the cardiac cycle. As illustrated in Fig. 3, a time-dependent mass-flow waveform was prescribed at the ICA inlet, while a physiological time-varying pressure waveform was imposed at the downstream outlets. The inlet waveform contains the characteristic acceleration, peak-systolic, deceleration, and diastolic phases of pulsatile arterial flow. The same inlet and outlet profiles were applied to the original and coiled models, ensuring that differences between the two simulations could be attributed to the presence of the coil-equivalent porous region.

The flow equations were solved using a pressure-based transient formulation with second-order temporal discretization and pressure–velocity coupling. A time step of 0.1 ms was employed to resolve transient variations during the cardiac waveform. Three complete cardiac cycles were simulated to minimize the influence of numerical initialization and establish a periodic flow response. Results from the final cardiac cycle were subsequently used for calculation of the hemodynamic quantities and generation of the snapshot datasets required by the ROM–TCN models. In particular, instantaneous pressure and WSS distributions were extracted, while OSI was determined from the temporal variation of the wall shear-stress vector. These datasets were then employed consistently in the POD-, PCA-, and Autoencoder-based dimensionality-reduction frameworks.

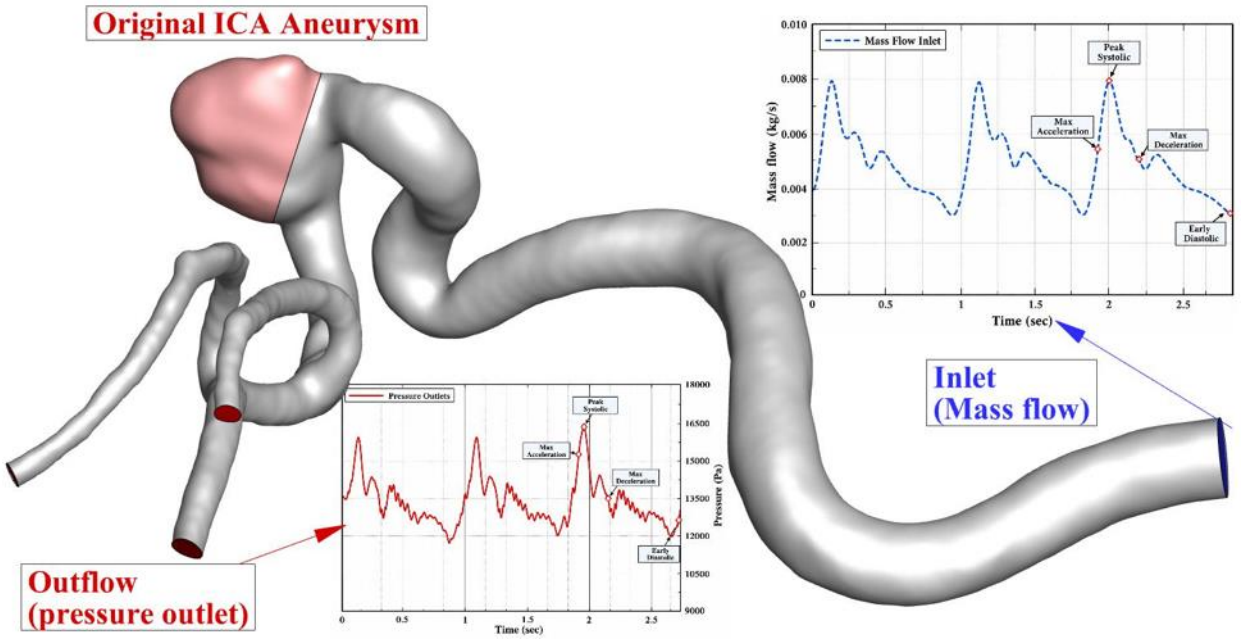

Fig. 3: Patient-specific computational domain and physiological boundary conditions used for the transient CFD simulations.

2.4. Computational Grid and Mesh Strategy

The computational domain was discretized using an unstructured mesh designed to resolve both the complex curvature of the ICA and the detailed geometry of the aneurysm sac. As demonstrated in Fig. 4, local mesh refinement was applied in the aneurysmal region, particularly near the aneurysm neck and wall, where large spatial variations in velocity and wall shear stress were expected. A comparatively coarser mesh was employed away from the aneurysm in portions of the parent vessel where the geometric and flow gradients were less severe. This nonuniform mesh strategy reduced the overall computational cost while maintaining enhanced spatial resolution in the regions most relevant to the hemodynamic analysis.

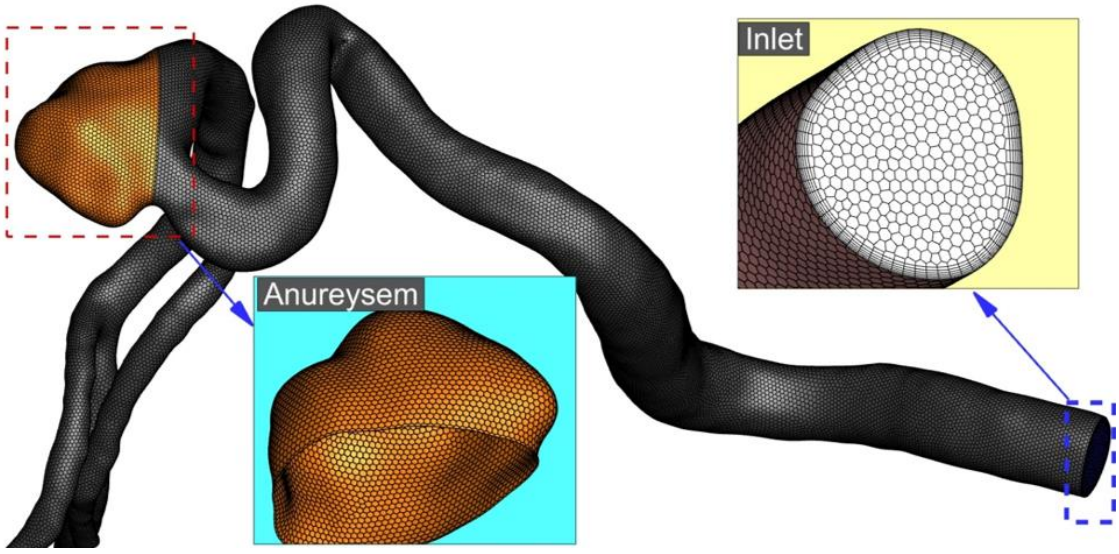

Fig. 4: Computational grid generated for the patient-specific ICA aneurysm.

Additional near-wall refinement was introduced to improve calculation of velocity gradients and WSS. The inlet cross-section was also adequately resolved to ensure accurate application and development of the prescribed pulsatile

inflow. For the coiled configuration, sufficient spatial resolution was maintained across the porous sac region and particularly near the interface between the parent-vessel flow and the porous aneurysm domain. Importantly, because the coils were modeled as an equivalent porous medium rather than explicitly as individual wires, the computational grid did not need to resolve the diameter or surface of each coil strand. This approach substantially reduces the cell count compared with an explicit coil-wire model while retaining the principal flow-resistance effect of the treatment.

3. Reduced-Order Modeling and Temporal Prediction Framework

To reduce the computational burden associated with high-dimensional transient CFD data and enable efficient prediction of aneurysmal hemodynamics, three dimensionality-reduction approaches—Principal Component Analysis (PCA), Autoencoder (AE), and Proper Orthogonal Decomposition (POD)—were independently combined with a common Temporal Convolutional Network (TCN). The overall architecture is illustrated in Fig. 5. For each hemodynamic variable considered in this study, namely pressure, WSS, and OSI, CFD snapshots obtained over the cardiac cycle were first arranged as a high-dimensional spatiotemporal dataset. Each ROM then compressed the spatial CFD fields into a substantially smaller set of time-dependent coefficients or latent variables. These reduced representations were supplied to the same TCN framework through sliding temporal windows to learn their temporal evolution. The TCN-predicted coefficients were subsequently transformed back into the physical domain using the corresponding inverse PCA transformation, Autoencoder decoder, or POD reconstruction procedure. Applying a common temporal predictor is important because it enables the differences in reconstruction and prediction performance to be primarily associated with the selected dimensionality-reduction strategy. The same procedure was applied independently to the original and coiled patient configurations, allowing the robustness of each ROM–TCN framework to be assessed before and after the substantial modification of intra-aneurysmal hemodynamics produced by coiling.

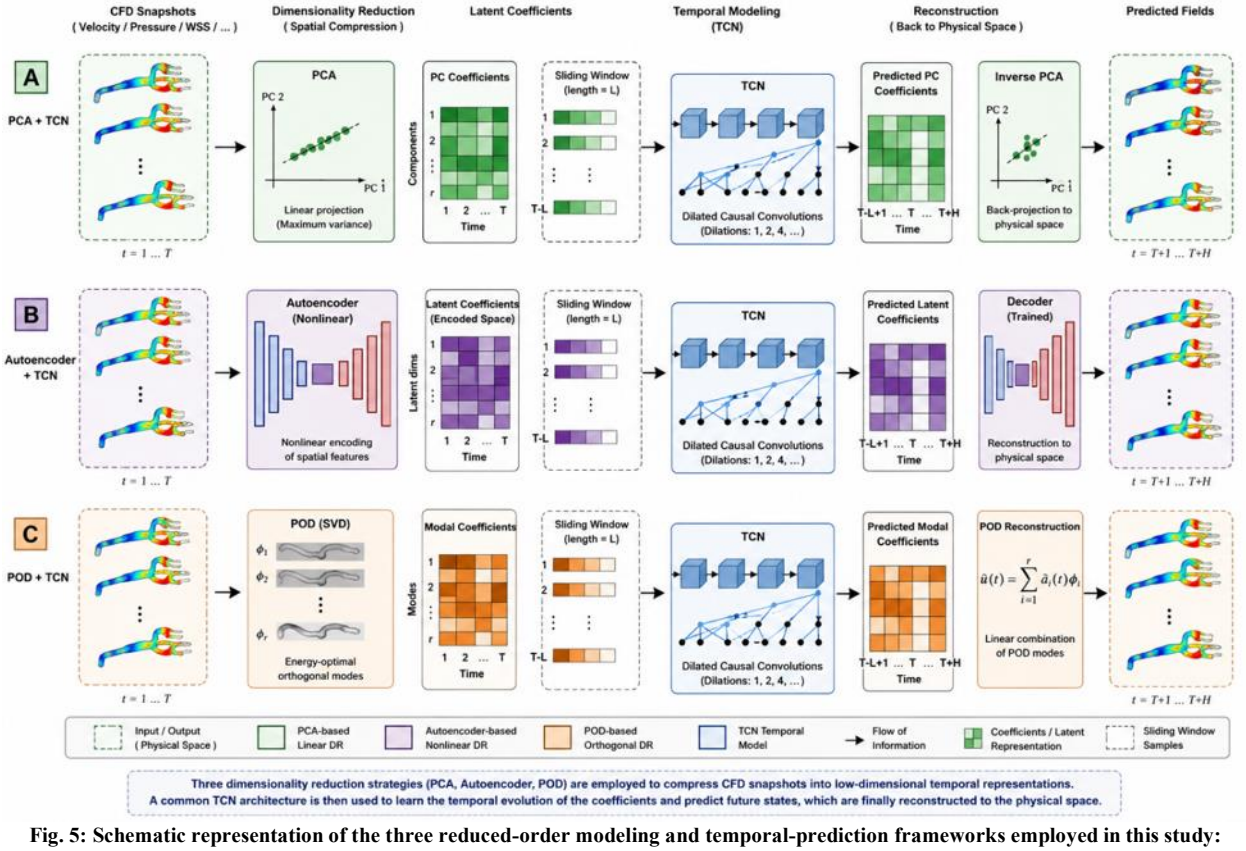

Fig. 5: Schematic representation of the three reduced-order modeling and temporal-prediction frameworks employed in this study: (A) PCA–TCN, (B) Autoencoder–TCN, and (C) POD–TCN.

3.1. . *Principal Component Analysis–TCN*

PCA provides a linear dimensionality-reduction technique in which the original CFD snapshots are projected onto a set of mutually orthogonal principal components that retain the directions of greatest variance in the dataset. For a snapshot matrix

$$\mathbf{X} = [\mathbf{x_1}, \mathbf{x_2}, \dots, \mathbf{x_T}] \in \mathbb{R}^{N \times T},$$

where N represents the number of spatial degrees of freedom and T is the number of temporal snapshots, the temporal mean is first calculated and removed,

$$\mathbf{X}' = \mathbf{X} - \overline{\mathbf{x}}.$$

The covariance matrix can then be expressed as

$$\mathbf{C} = \frac{\mathbf{1}}{\boldsymbol{T-1}} \mathbf{X}' \mathbf{X}'^{\boldsymbol{T}}.$$

Its eigenvectors define the principal directions, whereas the corresponding eigenvalues indicate the variance represented by individual components [32]. After retaining the first r components, the reduced representation is obtained as

$$\mathbf{Z_{PCA}} = \mathbf{W}_r^{\boldsymbol{T}} (\mathbf{X} - \overline{\mathbf{x}}),$$

where $\mathbf{W}_r$ contains the retained principal components. Thus, each instantaneous CFD field containing a very large number of spatial variables is replaced by only r PCA coefficients.

As illustrated in Fig. 5A, the temporal sequences of these coefficients were divided into sliding windows and supplied to the TCN. The network predicts the PCA coefficients corresponding to future time instances. The predicted physical field is recovered through inverse PCA transformation,

$$\hat{\mathbf{x}}(\boldsymbol{t}) = \overline{\mathbf{x}} + \mathbf{W}_r \hat{\mathbf{z}}_{\boldsymbol{PCA}}(\boldsymbol{t}).$$

The PCA-TCN framework therefore represents a fully linear spatial-compression approach combined with nonlinear temporal prediction.

3.2. Autoencoder-TCN

Unlike PCA, an Autoencoder provides a nonlinear representation of the CFD snapshots. As shown in Fig. 5B, the network consists of an encoder and a decoder. The encoder progressively transforms the high-dimensional input field into a compact latent vector,

$$\mathbf{z}(\boldsymbol{t}) = \boldsymbol{f}_{\mathbf{enc}}[\mathbf{x}(\boldsymbol{t}); \boldsymbol{\theta_e}],$$

where f_{enc} denotes the nonlinear encoder transformation, $\boldsymbol{\theta}_e$ represents its trainable parameters, and $\mathbf{z} \in \mathbb{R}^r$ is the reduced latent representation. The decoder performs the reverse transformation,

$$\tilde{\mathbf{x}}(\boldsymbol{t}) = \boldsymbol{f}_{\mathbf{dec}}[\mathbf{z}(\boldsymbol{t}); \boldsymbol{\theta_d}].$$

The Autoencoder is trained by minimizing the difference between the original CFD snapshot and its reconstructed counterpart [33]. A representative reconstruction objective is

$$\mathcal{L}_{AE} = \frac{1}{T} \sum_{t=1}^{T} \|\mathbf{x}(t) - \tilde{\mathbf{x}}(t)\|_2^2.$$

The principal advantage of this approach for aneurysmal flows is that the compression is not restricted to a linear subspace. The encoder can therefore represent nonlinear relationships among complex spatial structures, including localized WSS distributions and strongly heterogeneous intra-aneurysmal flow features.

Following training, only the latent coefficients associated with each CFD snapshot are used for temporal modeling. A sequence of latent vectors is supplied to the TCN, which predicts their future evolution. The predicted latent state, $\hat{\mathbf{z}}(t + \Delta t)$,

is then passed through the trained decoder to reconstruct the corresponding hemodynamic field,

$$\hat{\mathbf{x}}(\boldsymbol{t + \Delta t}) = \boldsymbol{f}_{\mathbf{dec}}[\hat{\mathbf{z}}(\boldsymbol{t + \Delta t})].$$

This Autoencoder-TCN combination consequently provides nonlinear compression in the spatial domain together with TCN-based temporal forecasting.

3.3. Proper Orthogonal Decomposition-TCN

POD provides a modal representation of the CFD field by identifying an orthogonal basis that optimally represents the energetic content of the available snapshots. The mean-subtracted snapshot matrix can be decomposed using singular value decomposition (SVD),

$\mathbf{X}' = \mathbf{U}\boldsymbol{\Sigma}\mathbf{V}^T$,

where the columns of U define the POD spatial modes, $\boldsymbol{\Sigma}$ contains the singular values, and $\mathbf{V}$ contains the associated temporal information [34]. The instantaneous field can then be approximated using the first r dominant modes,

$$\mathbf{x}(t) \approx \overline{\mathbf{x}} + \sum_{i=1}^{r} a_i(t)\boldsymbol{\phi}_i,$$

where $\boldsymbol{\phi}_i$ represents the i th POD mode and $a_i(t)$ is its corresponding temporal coefficient. The number of retained modes was determined according to the cumulative modal energy,

$$E_r = \frac{\sum_{i=1}^{r} \sigma_i^2}{\sum_{i=1}^{N} \sigma_i^2},$$

where σ_i denotes the i th singular value. Retaining the dominant modes removes low-contribution information while preserving the major spatial structures of the CFD solution.

As depicted in Fig. 5C, the resulting modal coefficients form a low-dimensional temporal sequence that is supplied to the TCN. After forecasting, the predicted modal coefficients are projected back into physical space according to

$$\hat{\mathbf{x}}(t) = \overline{\mathbf{x}} + \sum_{i=1}^{r} \hat{a}_i(t)\boldsymbol{\phi}_i.$$

POD therefore provides a compact and physically interpretable modal representation against which the PCA and nonlinear Autoencoder approaches can be compared.

3.4. ***3.4.*** *Temporal Convolutional Network (TCN)*

A common TCN architecture was adopted for all three ROM approaches to provide a consistent basis for temporal prediction. As illustrated in Fig. 5, the input to the TCN is not the original high-dimensional CFD field but a sequence of reduced PCA coefficients, Autoencoder latent variables, or POD modal coefficients. A sliding window of length L is constructed from the reduced temporal sequence,

$$\mathbf{Z}_{t-L+1:t} = \{\mathbf{z}_{t-L+1}, \dots, \mathbf{z}_t\},$$

and is used to estimate one or more subsequent reduced states,

$$\hat{\mathbf{z}}_{t+1:t+H} = F_{\mathrm{TCN}}(\mathbf{Z}_{t-L+1:t}),$$

where L is the input sequence length and H denotes the prediction horizon.The TCN employs causal convolutions, ensuring that the predicted state at a given time depends only on the current and previous observations and does not use information from future time steps. To capture temporal dependencies over a longer portion of the cardiac cycle without requiring an excessively deep network, dilated convolutions are employed. For a one-dimensional input sequence z, the dilated convolution can be expressed as

$$F(t) = \sum_{k=0}^{K-1} f(k)z(t - dk),$$

where K is the convolutional kernel size and d represents the dilation factor. Successively increasing dilation factors, such as $d = 1,2,4, \dots$, expand the effective receptive field and allow the network to learn both short- and longer-term temporal variations in the reduced hemodynamic representation [35].

Using an identical TCN concept for PCA, Autoencoder, and POD is particularly important for the objectives of the present study. It provides a controlled comparison in which all three methods receive CFD information from the same patient and predict the same hemodynamic variables, while differing primarily in how the original spatial fields are compressed and reconstructed. Furthermore, the analysis is performed for both the untreated original aneurysm and the coiled aneurysm, providing an additional test of whether each reduced representation can adequately capture and predict the different hemodynamic environments before and after intervention.

4. Results and Discussion

4.1. Effect of Endovascular Coiling on Intra-Aneurysmal Flow Structure

Figure 6 illustrates the substantial modification of the intra-aneurysmal flow structure induced by endovascular coiling. In the original untreated aneurysm, the incoming blood flow penetrates deeply into the sac and develops a complex three-dimensional circulation characterized by numerous high-velocity streamlines, strong flow turning, and

extensive recirculation throughout the aneurysmal cavity. Local velocities approaching the upper range of the scale (~0.9 m/s) are observed along portions of the inflow pathway, indicating considerable momentum transfer from the parent vessel into the sac. Following endovascular coiling, the porous resistance introduced within the aneurysm markedly attenuates this penetration and dissipates the momentum of the incoming jet. Consequently, the number of high-velocity trajectories inside the sac is substantially reduced, while a larger portion of the aneurysmal volume is occupied by low-velocity flow, particularly toward the dome and peripheral regions. The streamline patterns also become less energetic and less extensively distributed within the sac compared with the untreated configuration. These observations demonstrate that coiling acts primarily by increasing hydraulic resistance within the aneurysm, thereby suppressing intra-sac circulation and partially isolating the aneurysmal cavity from the energetic parent-vessel flow. Such pronounced alteration of the underlying flow field is also important for the subsequent ROM analysis because the POD, PCA, and Autoencoder models must represent two distinctly different hemodynamic states using compact reduced-dimensional representations.

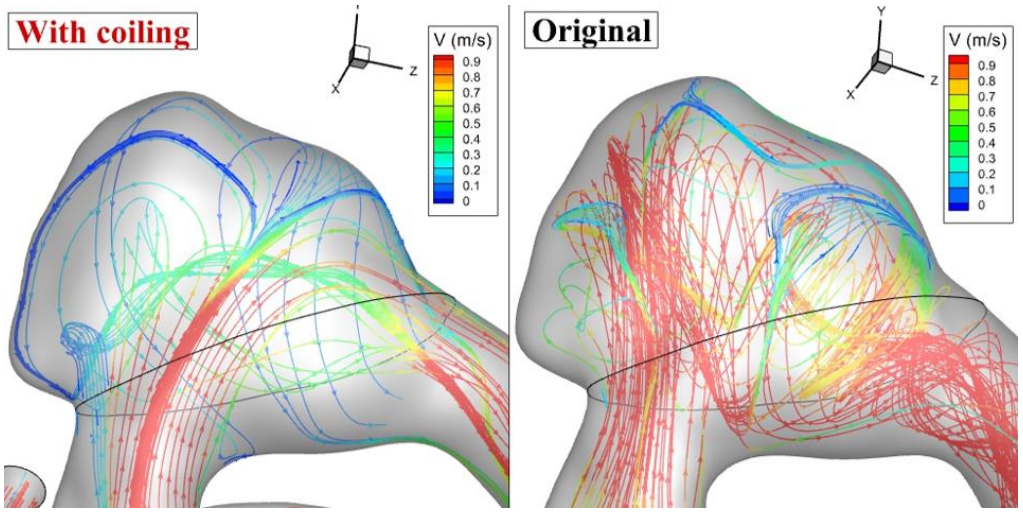

Fig. 6. Comparison of velocity-colored streamlines within the patient-specific ICA aneurysm before (original) and after endovascular coiling, illustrating the suppression of intra-aneurysmal flow penetration and circulation induced by the coil-equivalent porous region

4.2. Evaluation of Dimensionality Reduction and Selection of Retained Modes

Figure 7 compares the dimensionality-reduction behavior of POD, PCA, and Autoencoder (AE) for the three target hemodynamic quantities, namely OSI, pressure, and AWSS, in both the original and coiled aneurysm configurations. A 99% information-retention threshold was adopted to determine a sufficiently compact representation while preserving the dominant characteristics of the CFD fields. The results reveal clear differences among both the hemodynamic variables and reduction techniques. For POD, OSI and pressure exhibit very rapid convergence, with only a few dominant modes accounting for almost all of the field information. AWSS shows a slower accumulation, particularly for the original aneurysm, indicating a more spatially complex distribution that requires a larger modal basis. Coiling also modifies the modal-energy distribution; most notably, the AWSS curve for the coiled configuration rises more rapidly than that of the original case, suggesting that suppression of complex intra-aneurysmal circulation concentrates the wall-shear dynamics into fewer dominant structures. The PCA results show a similar overall tendency, with OSI and pressure approaching the 99% threshold using only a small number of principal components, whereas AWSS again requires a larger reduced space. This behavior confirms that the wall-shear field contains richer spatial variations than pressure and OSI and is therefore more demanding to compress.

The Autoencoder exhibits a somewhat different convergence pattern because its latent variables represent a nonlinear encoding rather than orthogonal modes ranked strictly by modal energy or variance. As shown in Fig. 7(c), pressure and OSI can be represented with relatively few latent dimensions, while AWSS requires a progressively larger latent space to reach the prescribed information-retention level. The distinction between the original and coiled configurations is also apparent, demonstrating that the change in flow topology induced by coiling affects the complexity of the reduced representation. Nevertheless, all three approaches approach or exceed the 99% threshold within approximately 10 reduced dimensions, indicating that the high-dimensional CFD datasets possess substantial redundancy and can be represented using a comparatively compact latent space. Based on these results, 10 retained dimensions were selected for POD, PCA, and Autoencoder in the subsequent TCN analysis. Using the same reduced

dimension for all three methods also establishes a consistent basis for comparing their reconstruction and temporal-prediction performance, ensuring that differences among POD–TCN, PCA–TCN, and Autoencoder–TCN are not simply caused by using different latent-space sizes.

a)

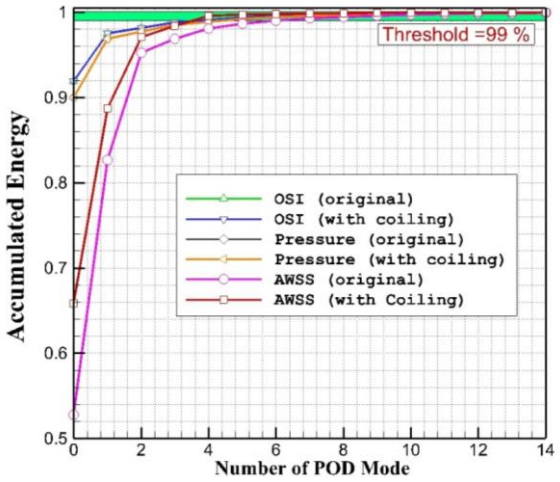

b)

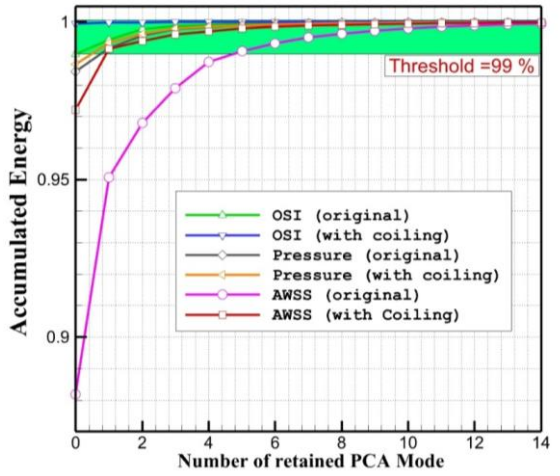

c)

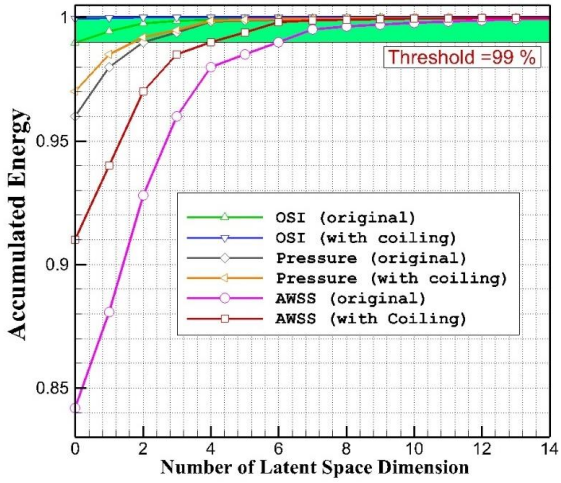

Fig. 7. Accumulated information/energy as a function of the reduced-space dimension for the original and coiled aneurysm configurations using (a) POD modes, (b) PCA components, and (c) Autoencoder latent-space dimensions..

4.3. Reconstruction Accuracy of POD, PCA, and Autoencoder Models

Figure 8 compares the reconstruction errors of the POD, PCA, and Autoencoder models for the principal hemodynamic quantities in the original and coiled aneurysm configurations over the cardiac cycle. In general, the reconstruction error is strongly dependent on the hemodynamic variable, demonstrating that the ability of a reduced-order representation to recover the CFD solution is governed by the spatial complexity and temporal variability of the underlying field. Pressure exhibits the lowest and most stable reconstruction error, consistent with its relatively smooth spatial distribution and the rapid information convergence observed in Fig. 7. In contrast, WSS/AWSS and OSI are more difficult to reconstruct, because they are highly sensitive to local velocity gradients, near-wall flow structures, flow separation, and recirculation within the aneurysm sac. Consequently, relatively small discrepancies in the reconstructed velocity-related structures can produce more noticeable errors in these wall-based parameters.

Comparison of the three ROM approaches further demonstrates the influence of the selected dimensionality-reduction strategy. POD and PCA provide compact linear representations and reproduce the dominant global characteristics of the CFD fields effectively, particularly for pressure. Their reconstruction errors arise primarily from truncating the higher-order modes/components, which contain lower-energy but potentially important localized spatial information. The Autoencoder differs fundamentally because its nonlinear encoder–decoder structure is able to map the CFD fields onto a nonlinear latent manifold, providing greater flexibility for representing spatially heterogeneous hemodynamic patterns. Nevertheless, its reconstruction quality also depends on the adequacy of the latent-space dimension and the training of the encoder and decoder; therefore, nonlinear compression does not automatically guarantee lower error at every instant or for every variable. The temporal fluctuations visible in Fig. 8 indicate that reconstruction accuracy also varies throughout the cardiac cycle, with larger deviations tending to occur during phases characterized by stronger changes in the underlying flow field.

A further important observation is the difference between the original and coiled aneurysm. As demonstrated previously by the streamline comparison in Fig. 6, coiling substantially suppresses the energetic intra-sac circulation and changes the spatial organization of the flow. These changes modify the dimensional complexity of the hemodynamic fields and, consequently, their reconstruction behavior. The differences between the original and coiled error curves therefore indicate that ROM performance is not determined solely by the reduction algorithm but also by the physical state being represented. In particular, the more organized and attenuated intra-aneurysmal flow produced by the porous coil region can concentrate the dominant dynamics into a smaller number of structures for some variables, whereas sharp local gradients near the neck and the transition between the parent vessel and treated sac may remain challenging to reconstruct. Overall, Fig. 8 demonstrates that the selected reduced representations preserve the principal characteristics of the CFD solutions while reducing the original high-dimensional fields to only 10 reduced variables. The reconstruction assessment is especially important because these reconstructed reduced states form the basis for the subsequent TCN prediction; thus, the final accuracy of the hybrid POD–TCN, PCA–TCN, and Autoencoder–TCN models reflects both the intrinsic ROM reconstruction error and the additional error introduced during temporal forecasting.

a)

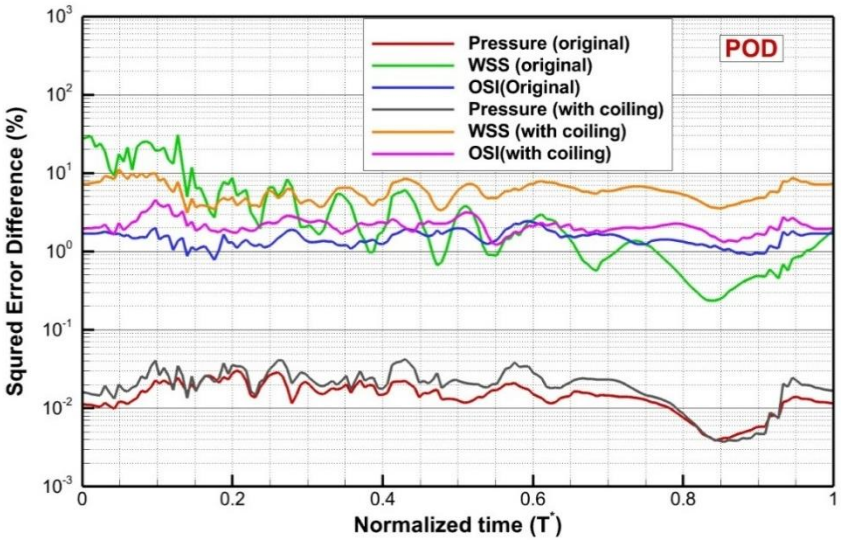

b)

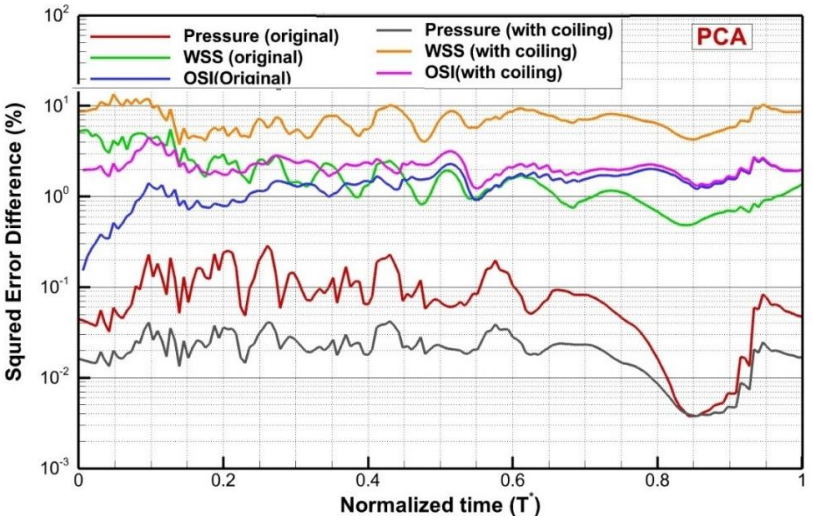

c)

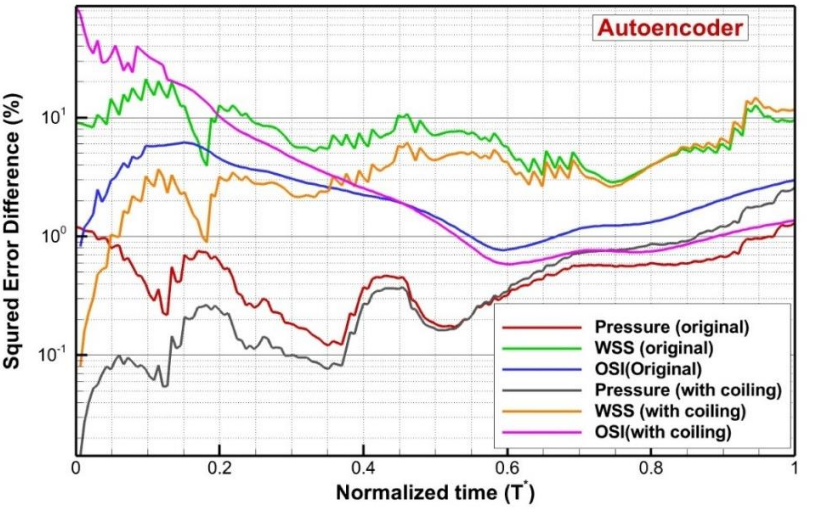

Fig. 8. Reconstruction errors of the a) POD, b) PCA, and c)Autoencoder reduced-order models for the principal hemodynamic quantities over the cardiac cycle in the original and coiled patient-specific aneurysm configurations. Ten reduced dimensions are retained for each ROM according to the dimensionality analysis presented in Fig. 7.

4.4. 4.4. Prediction Performance of the ROM–TCN Models

Figure 9 compares the reconstruction and temporal prediction errors obtained using the PCA–TCN, POD–TCN, and Autoencoder–TCN frameworks for OSI, pressure, and WSS in the original and coiled aneurysm configurations. The prediction interval begins at a normalized time of approximately 0.76, as indicated by the shaded region. A common feature of all three approaches is the clear increase in error when transitioning from reconstruction to forecasting. During reconstruction, the ROMs operate on states represented within their learned reduced spaces, whereas in the prediction interval the TCN must extrapolate the temporal evolution of the reduced coefficients without access to the subsequent CFD states. Consequently, prediction uncertainty accumulates with increasing forecasting horizon. The magnitude of this increase is strongly dependent on both the selected ROM and the hemodynamic variable, demonstrating that accurate spatial compression does not necessarily guarantee equally accurate long-horizon temporal prediction.

For PCA–TCN, relatively low reconstruction errors are observed for pressure and OSI before the prediction boundary, while WSS remains more difficult to reconstruct because of its greater spatial complexity and sensitivity to local near-wall gradients. Once forecasting begins, the errors increase progressively for all three variables. In particular, OSI and WSS exhibit pronounced growth toward the end of the prediction interval, whereas pressure shows a lower absolute error but also displays a clear increasing trend. Comparison of the original and coiled configurations

indicates that the coiled case generally follows the same temporal evolution but with somewhat lower errors over substantial portions of the prediction interval. This behavior is consistent with the flow-field observations in Fig. 6: the porous coil region suppresses energetic intra-aneurysmal circulation and produces a more organized flow environment, which can reduce the temporal complexity that must be represented by the PCA coefficients and subsequently extrapolated by the TCN.

The POD–TCN model also exhibits a distinct difference between the reconstruction and forecasting intervals. Errors decrease substantially throughout the reconstruction region as the dominant modal structures represent the evolving CFD solution, but increase after the TCN begins forecasting the modal coefficients. WSS presents the largest prediction errors, followed by OSI, whereas pressure generally remains less sensitive. The strong fluctuations observed during portions of the reconstructed interval reflect the sensitivity of the instantaneous error to different phases of the cardiac cycle. Nevertheless, the similarity between the temporal trends of the original and coiled cases suggests that the POD basis preserves the principal dynamics of both configurations. The coiled case again tends to exhibit lower errors than the untreated configuration in several regions, which can be associated with the attenuation of complex recirculation and high-gradient structures following treatment.

The Autoencoder–TCN framework demonstrates a different error distribution because the CFD fields are represented on a nonlinear latent manifold rather than through a linear modal projection. Reconstruction errors generally decrease considerably as normalized time advances, particularly for OSI and pressure, indicating that the nonlinear encoder–decoder can compactly represent the dominant structures of the training data. However, a substantial increase occurs at the beginning of the prediction interval, followed by progressive error growth for several quantities as the forecasting horizon increases. WSS again represents one of the most demanding quantities because localized shear structures are highly sensitive to errors in the predicted latent state. The comparison also shows differences between the original and coiled configurations, indicating that modification of the underlying flow topology affects not only spatial reconstruction but also the temporal evolution learned within the latent space.

Taken together, Fig. 9 demonstrates that pressure is generally easier to reconstruct and temporally forecast than the wall-derived quantities, whereas WSS and OSI impose a more demanding test on the ROM–TCN frameworks because of their localized and strongly time-dependent characteristics. More importantly, the comparison highlights two distinct sources of surrogate-model error: the error introduced when the CFD field is compressed and reconstructed by the ROM and the additional error generated when the TCN forecasts the reduced coordinates beyond the training interval. The progressive error growth within the prediction region therefore indicates that long-horizon temporal extrapolation is the principal challenge, even when the reduced representation itself provides satisfactory reconstruction. The differences between the original and coiled cases further demonstrate that treatment-induced changes in flow complexity directly influence surrogate-model performance. These findings support evaluating POD, PCA, and Autoencoder not solely according to their dimensional compression capability, but according to the combined accuracy of compression, physical-field reconstruction, and temporal forecasting when selecting an efficient ROM for patient-specific aneurysm hemodynamics.

a)

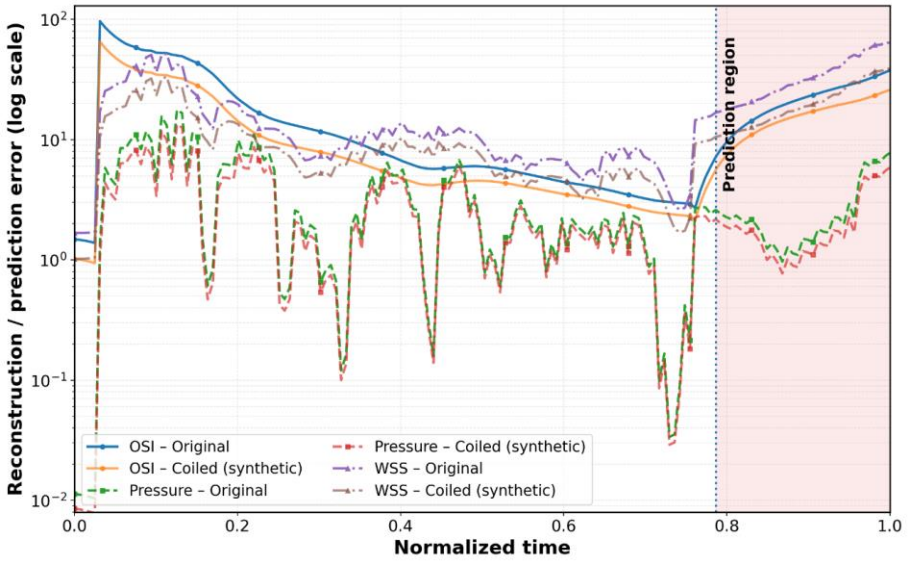

b)

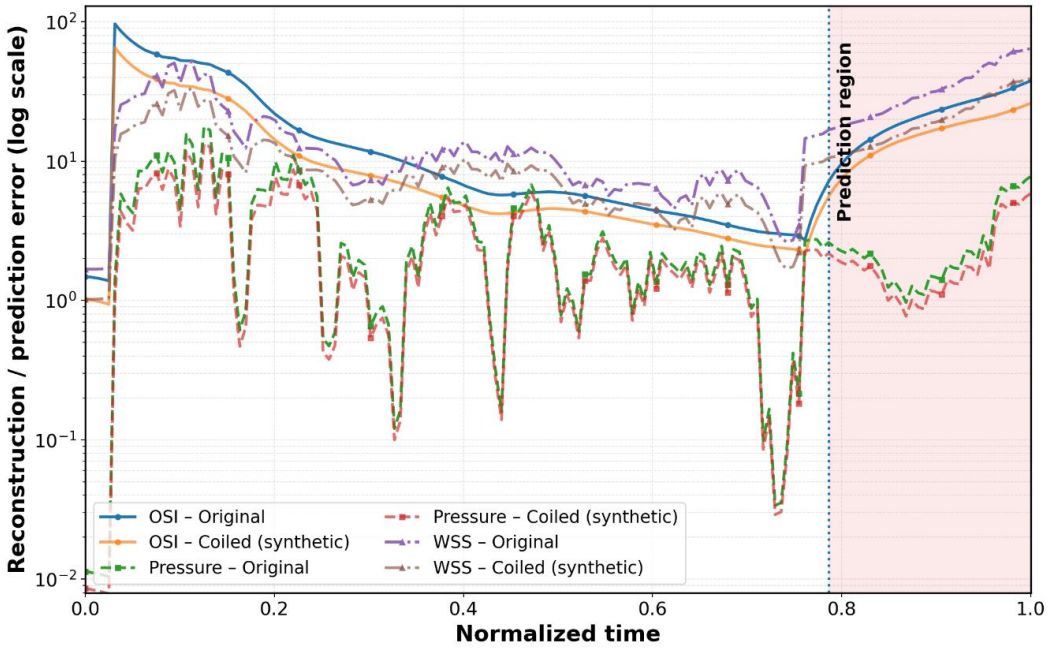

c)

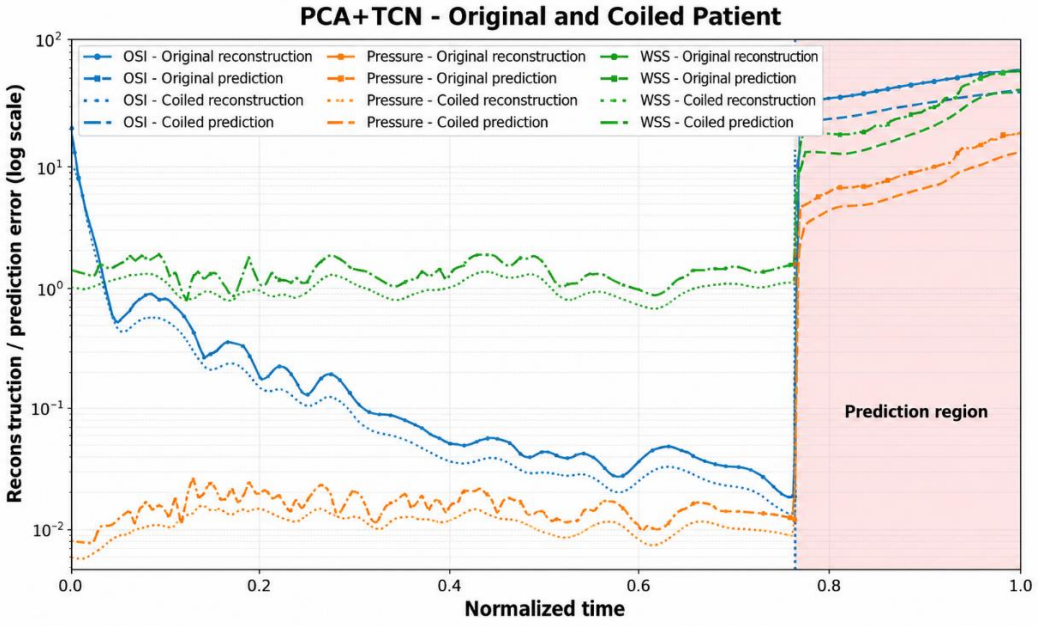

Fig. 9. Reconstruction and prediction errors of the PCA–TCN, POD–TCN, and Autoencoder–TCN frameworks for OSI, pressure, and WSS over the normalized cardiac cycle for the original and coiled patient-specific ICA aneurysm.

Based on the prediction-error trends in Fig. 9, PCA–TCN shows the strongest overall predictive performance for the present dataset, particularly when the stability of the prediction error across OSI, pressure, and WSS is considered together. PCA provides a compact linear representation in which the dominant variance of the hemodynamic fields is concentrated into a small number of temporally coherent coefficients, making their evolution comparatively easier for the TCN to learn and extrapolate. POD–TCN also captures the dominant flow structures effectively, but its prediction errors exhibit stronger temporal fluctuations, particularly for the wall-related quantities. The Autoencoder–TCN benefits from nonlinear spatial compression and achieves effective reconstruction, yet its prediction errors increase substantially during the forecasting interval, especially for WSS, suggesting that the nonlinear latent variables are more difficult for the TCN to extrapolate over a long prediction horizon. Therefore, for the investigated patient-specific aneurysm and the adopted training–prediction configuration, PCA–TCN provides the most stable balance

between dimensionality reduction and temporal forecasting, while the results also demonstrate that good reconstruction accuracy alone does not necessarily translate into superior prediction performance.

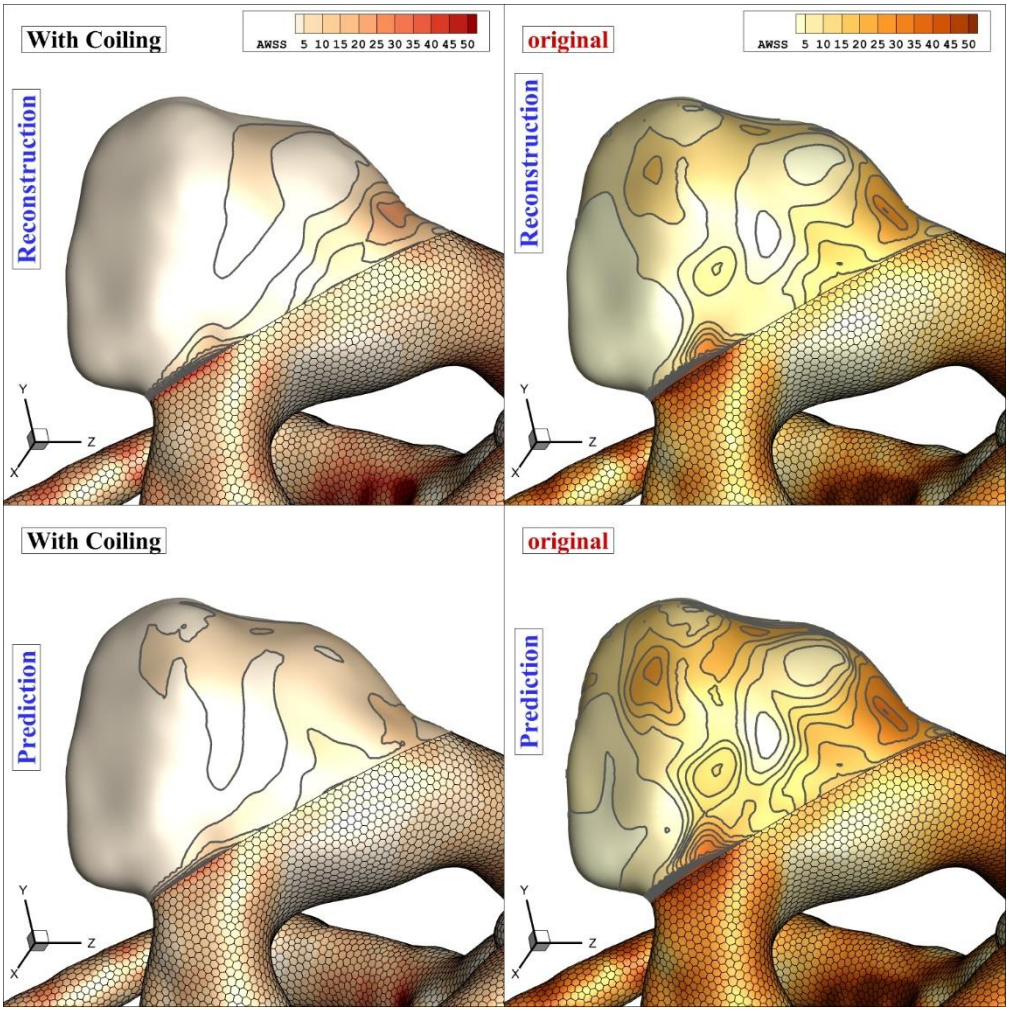

Fig. 10. Comparison of reconstructed and PCA–TCN-predicted average wall shear stress (AWSS) distributions at peak systole for the patient-specific ICA aneurysm with and without endovascular coiling

At the peak-systolic phase, the PCA–TCN framework demonstrates good capability in reproducing the spatial distribution of AWSS for both the original and coiled aneurysm configurations (Fig. 10). For the original aneurysm, the predicted field successfully preserves the major heterogeneous AWSS structures observed in the reconstructed result, including the elevated shear region concentrated near the aneurysm neck and the lower-to-moderate AWSS zones distributed over the sac surface. The prediction also reproduces the characteristic spatial gradients and localized contour structures across the aneurysm, although some differences in the extent and intensity of individual high- and low-AWSS regions remain. Following coiling, the AWSS distribution becomes considerably more uniform and generally weaker over the aneurysm sac, consistent with the attenuation of intra-sac flow and inflow momentum by the porous coil region. The PCA–TCN prediction closely reproduces this smoother post-coiling pattern, including the low-AWSS region over most of the sac and the relatively higher values concentrated near the neck. Overall, the close qualitative agreement between reconstructed and predicted fields indicates that PCA–TCN captures not only the magnitude range but, more importantly, the treatment-induced redistribution of AWSS at peak systole, with the less spatially complex coiled field appearing particularly well represented by the predictive model.

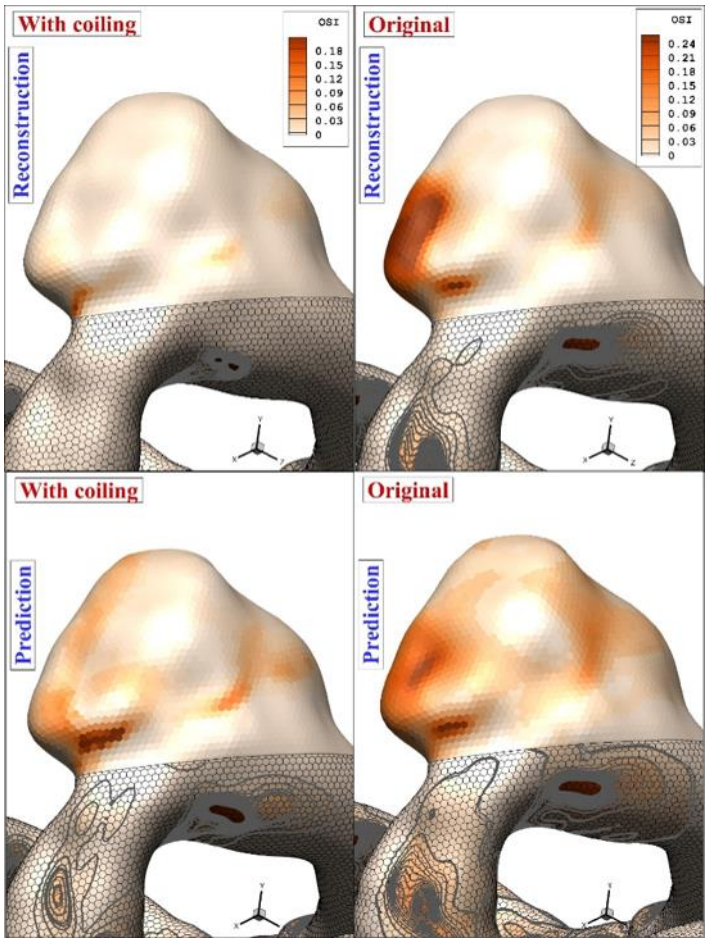

Fig. 11. Comparison of reconstructed and PCA–TCN-predicted oscillatory shear index (OSI) distributions for the original and endovascularly coiled patient-specific ICA aneurysm

Figure 11 compares the OSI reconstruction and PCA–TCN prediction for the original and coiled aneurysm configurations. For the original aneurysm, the reconstructed field exhibits pronounced spatial heterogeneity, with relatively high OSI concentrated along the lateral sac surface and near the neck, indicating regions exposed to stronger temporal oscillation of wall shear stress. The PCA–TCN prediction successfully reproduces the principal locations and overall spatial organization of these elevated-OSI regions, although some differences in their local extent and intensity are visible. Endovascular coiling substantially modifies the OSI distribution, with the reconstructed coiled case showing generally lower OSI over most of the sac and elevated values restricted mainly to localized regions near the neck and lower sac surface. The PCA–TCN prediction captures this overall post-coiling pattern and the dominant low-OSI area, while slightly expanding or intensifying some localized elevated-OSI regions. Thus, despite local discrepancies, the close qualitative correspondence between reconstruction and prediction demonstrates that PCA–TCN preserves the major spatial characteristics of OSI and distinguishes the substantially different oscillatory shear environments of the original and coiled aneurysms.

At the peak-systolic phase, Fig. 12 demonstrates that the PCA–TCN framework effectively predicts the principal spatial characteristics of the total-pressure field in both the original and coiled aneurysm configurations. In the original aneurysm, the reconstructed pressure field exhibits a relatively smooth distribution over the sac, with a localized higher-pressure region associated with the impingement of the incoming flow and gradual pressure variation toward the peripheral sac regions. The PCA–TCN prediction successfully reproduces the location and overall morphology of this dominant pressure structure, although some differences are visible in the size and intensity of individual contour regions. Following endovascular coiling, the pressure field is markedly redistributed because the porous coil region increases resistance to intra-aneurysmal flow and attenuates momentum penetration into the sac. Despite this treatment-induced change, the predicted coiled field retains the major pressure-gradient direction and identifies the principal elevated-pressure region observed in the reconstruction. Compared with WSS and OSI, pressure displays a

smoother spatial distribution, which is consistent with its lower-dimensional behavior and makes its dominant structures more readily represented by PCA and forecast by the TCN. Overall, the qualitative agreement between reconstruction and prediction indicates that PCA–TCN successfully captures the principal peak-systolic pressure patterns in both untreated and coiled configurations, while the remaining local contour differences reflect the accumulated uncertainty associated with temporal forecasting.

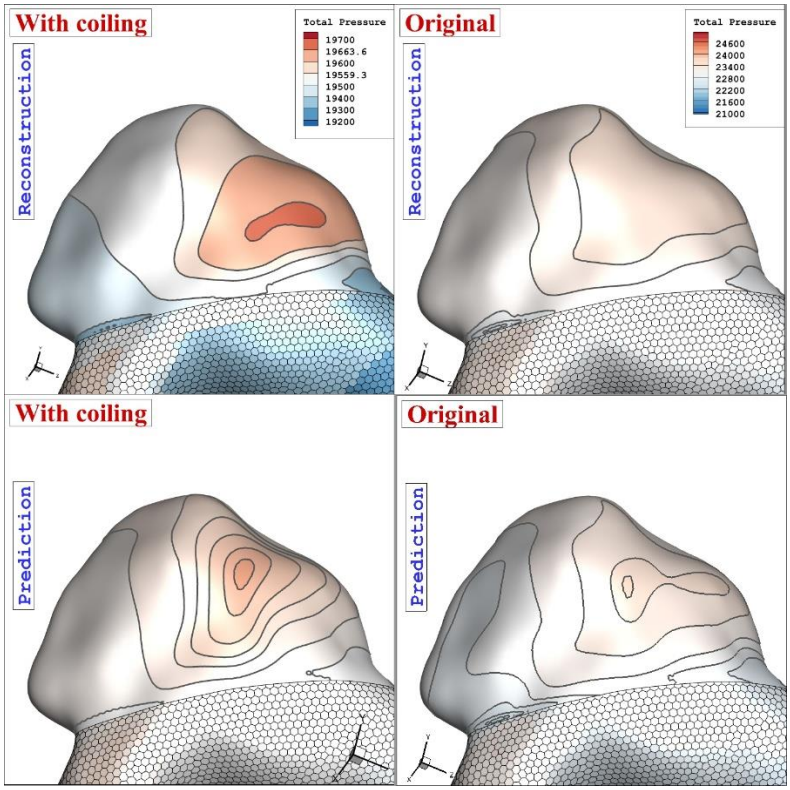

Fig. 12. Comparison of reconstructed and PCA–TCN-predicted total-pressure distributions at peak systole for the original and endovascularly coiled patient-specific ICA aneurysm

5. Conclusion

This study developed and compared three hybrid reduced-order modeling frameworks—POD–TCN, PCA–TCN, and Autoencoder–TCN—for efficient reconstruction and temporal prediction of patient-specific cerebral aneurysm hemodynamics before and after endovascular coiling. Transient CFD simulations of an ICA saccular aneurysm were performed under pulsatile conditions, while the coiled sac was represented using an equivalent porous-medium model. The analysis focused on clinically and biomechanically relevant hemodynamic quantities, including wall shear stress (WSS/AWSS), oscillatory shear index (OSI), and pressure. The principal conclusions are summarized as follows:

- Endovascular coiling substantially altered the intra-aneurysmal flow structure. The porous coil region suppressed penetration of the high-momentum inflow into the sac, reduced energetic recirculation, and produced a more quiescent flow environment, particularly toward the aneurysm dome. These flow modifications resulted in clear redistribution of the wall-based hemodynamic quantities compared with the untreated aneurysm.
- The dimensionality analysis demonstrated that the high-dimensional CFD fields could be represented using a relatively small reduced space. POD and PCA rapidly concentrated the dominant information into the first few modes/components, particularly for pressure and OSI, whereas AWSS required a larger reduced representation because of its stronger spatial heterogeneity and sensitivity to near-wall flow structures. The Autoencoder also provided effective nonlinear compression, although the required latent-space dimension depended on the complexity of the target variable.
- A common reduced dimension of 10 was sufficient to retain approximately 99% of the dominant information for the investigated fields and provided a consistent basis for comparing the three ROM approaches. The differences between the original and coiled cases further demonstrated that

treatment-induced modification of the flow topology changes the dimensional complexity of the hemodynamic fields.

- All three ROMs provided effective reconstruction of the principal CFD structures, although reconstruction accuracy varied according to the hemodynamic variable. Pressure was generally easier to represent because of its comparatively smooth spatial distribution, whereas WSS/AWSS and OSI were more demanding because of their localized gradients and sensitivity to complex near-wall flow behavior.
- Coupling the reduced representations with TCN enabled prediction beyond the reconstruction/training interval. Prediction errors increased with forecasting horizon for all three approaches, demonstrating that temporal extrapolation represents a more demanding task than spatial reconstruction. The results also show that a ROM with good reconstruction capability does not necessarily provide the most predictable latent dynamics.
- Among the investigated frameworks, PCA–TCN exhibited the most stable predictive behavior for the present dataset, providing a favorable balance between compact spatial representation and temporal predictability of the reduced coefficients. The peak-systolic contour comparisons further showed that PCA–TCN reproduced the principal spatial distributions of AWSS, OSI, and pressure and captured the major differences between the original and coiled aneurysm states.

Overall, the results demonstrate the potential of combining dimensionality reduction with temporal deep learning to construct computationally efficient surrogate models of patient-specific aneurysm hemodynamics. In particular, the comparison highlights that the choice of ROM should consider not only compression and reconstruction accuracy but also the temporal predictability of the resulting reduced coordinates. The PCA–TCN framework provides a promising approach for rapidly estimating transient hemodynamic fields in both untreated and treated aneurysms after training on high-fidelity CFD data. Nevertheless, the present conclusions are based on a single patient-specific geometry and a porous-medium representation of coiling. Future studies should therefore include larger patient cohorts, different aneurysm locations and morphologies, variable coil-packing conditions, patient-specific boundary conditions, and deformable vessel walls, together with external validation, to determine the generalizability of the proposed framework for broader cerebrovascular applications.

References

[1] Rostamian, Ali, Keivan Fallah, and Yasser Rostamiyan. "Reduction of rupture risk in ICA aneurysms by endovascular techniques of coiling and stent: Numerical study." Scientific Reports 13, no. 1 (2023): 7216.

[2] Jiang, Hao, Zhiwei Lu, M. Barzegar Gerdroodbary, Amir Sabernaeemi, and Sajad Salavatidezfouli. "The influence of sac centreline on saccular aneurysm rupture: computational study." Scientific Reports 13, no. 1 (2023): 11288.

[3] Shiryanpoor, Iman, Peiman Valipour, M. Barzegar Gerdroodbary, A. M. Abazari, and Rasoul Moradi. "Using computational fluid dynamic for evaluation of rupture risk of micro cerebral aneurysms in the growth process: hemodynamic analysis." International Journal of Modern Physics *C*, **36**(02) (2025): 2450184.

[4] Bozorgpour, Reza, Pilhwan Kim, and Mohammadreza Soltany Sadrabadi. "Hemodynamic variables in cerebral Aneurysms: integrating CFD-based computational modeling and clinical insight." *Brain Hemorrhages* (2026).

[5] Mousavi, S. Valiallah, Mostafa Barzegar Gerdroodbary, Amir Sabernaeemi, Sajad Salavatidezfouli, and Peiman Valipour. "Impacts of the aneurysm deformation induced by stent on hemodynamic of blood flow in saccular internal carotid artery aneurysms." AIP Advances 14, no. 9 (2024).

[6] Mantha, A., Christof Karmonik, G. Benndorf, C. Strother, and Ralph Metcalfe. "Hemodynamics in a cerebral artery before and after the formation of an aneurysm." American Journal of Neuroradiology 27, no. 5 (2006): 1113-1118.

[7] Jin, Zan-Hui, M. Barzegar Gerdroodbary, P. Valipour, M. Faraji, and Nidal H. Abu-Hamdeh. "CFD investigations of the blood hemodynamic inside internal cerebral aneurysm (ICA) in the existence of coiling embolism." *Alexandria Engineering Journal* 66 (2023): 797-809.

[8] Sabernaeemi, A., M. Barzegar Gerdroodbary, S. Salavatidezfouli, et al. "Influence of stent-induced vessel deformation on hemodynamic feature of bloodstream inside ICA aneurysms." Biomechanics and Modeling in Mechanobiology (2023). https://doi.org/10.1007/s10237-023-01710-9

[9] Munarriz, Pablo M., Pedro A. Gómez, Igor Paredes, Ana M. Castaño-Leon, Santiago Cepeda, and Alfonso Lagares. "Basic principles of hemodynamics and cerebral aneurysms." World Neurosurgery 88 (2016): 311-319.

[10] Song, Li, Peng Du, and Erhao Bao. "Influence of bleb formation on intracranial aneurysm hemodynamics: a patient-specific CFD study." Chinese Journal of Physics (2025).
[11] S. Valiallah Mousavi, M. Barzegar Gerdroodbary , Iman Shiryanpoor, Peiman Valipour, Hemodynamic Assessment of Bleb Formation in Patient-Specific Intracranial Aneurysms using Computational Fluid Dynamics, *International Journal of Modern Physics C* (2027) https://doi.org/10.1142/S0129183127501683.
[12] Rajab, Husam, Joy Djuansjah, Saman Ahmad Aminian, Hana Ihsan Hassan, Hiba Mushtaq, Waam Mohammed Taher, Mariem Alwan, and Rashid Khan. "Computational characterization of geometry-driven hemodynamics in intracranial aneurysms." The European Physical Journal Plus 141, no. 3 (2026): 312.
[13] Barzegar Gerdroodbary, Mostafa, and Li-Cai Zhao. "Investigation of Pulsatile Blood Flow Dynamics in Anterior Cerebral Artery Aneurysms under Different Physiological Conditions: Hemodynamic Analyses." Journal of Applied and Computational Mechanics (2025): e19553.
[14] Cebral, Juan R., Alessandro Radaelli, Alejandro Frangi, and Christopher M. Putman. "Hemodynamics before and after bleb formation in cerebral aneurysms." In Medical Imaging 2007: Physiology, Function, and Structure from Medical Images, vol. 6511, pp. 725-733. SPIE, 2007.
[15] Bozorgpour, Reza. "Hemodynamic markers: CFD-based prediction of cerebral aneurysm rupture risk." *Vascular Pharmacology* (2025): 107578..
[16] Satoh, Toru. "Hemodynamic analysis of a thrombosed bleb in an unruptured cerebral aneurysm." Surgical Neurology International 15 (2024): 357.
[17] Barzegar Gerdroodbary, M., and X. Wang."A Computational Analysis of Sac Volume Effects on Hemodynamics and Rupture Risk in Cerebral Saccular Aneurysms."Journal of Applied and Computational Mechanics, 12(3) (2026), pp. 1084–1092.
[18] Chatziprodromou, I., V. Butty, V. B. Makhijani, D. Poulikakos, and Y. Ventikos. "Pulsatile blood flow in anatomically accurate vessels with multiple aneurysms: a medical intervention planning application of computational haemodynamics." Flow, Turbulence and Combustion 71 (2003): 333-346.
[19] Cornelissen, B. M. W., J. J. Schneiders, W. V. Potters, R. Van Den Berg, B. K. Velthuis, G. J. E. Rinkel, C. H. Slump, E. VanBavel, C. B. L. M. Majoie, and H. A. Marquering. "Hemodynamic differences in intracranial aneurysms before and after rupture." American Journal of Neuroradiology 36, no. 10 (2015): 1927-1933.
[20] Barzegar Gerdroodbary, M., and S. Salavatidezfouli. "Predictive surrogate model based on linear and nonlinear solution manifold reduction in cardiovascular FSI: A comparative study." Computers in Biology and Medicine 189 (2025): 109959. https://doi.org/10.1016/j.compbiomed.2025.109959
[21] Hammouda, Nadia Ghezaiel, Joy Djuansjah, Ali BM Ali, As'ad Alizadeh, Muntadher Abed Hussein, Narinderjit Singh Sawaran Singh, Khalil Hajlaoui, and Walid Aich. "Patient-specific deep learning reduced-order model of blood hemodynamic indices in thoracic aortic aneurysms via dynamic mode decomposition." Chinese Journal of Physics (2025).
[22] Kheiri, Amir, Saman Hariri, M. Barzegar Gerdroodbary, Maryam Sorkhi, and Peiman Valipour. "A CFD–Machine Learning Framework for Efficient Prediction of Cerebral Aneurysm Hemodynamic under Vessel Dilation." Chinese Journal of Physics 102 (2026): 748-767. https://doi.org/10.1016/j.cjph.2026.04.015
[23] Hammouda, Nadia Ghezaiel, Karim Kriaa, As'ad Alizadeh, Husam Rajab, Abdellatif M. Sadeq, Narinderjit Singh Sawaran Singh, Khalil Hajlaoui, and Walid Aich. "Physically informed machine learning for predicting non-Newtonian blood flow in Giant MCA aneurysms after endovascular treatment." International Communications in Heat and Mass Transfer 172 (2026): 110296.
[24] Liang, Meiling, Jiacheng Liu, Hao Wang, Shizhe An, Chaonan Chen, Hanbing Chu, Mingting Zhu, et al. "Ultrasound super-resolved hemodynamic estimation in microvessel using physics-informed neural networks and data assimilation." Computer Methods and Programs in Biomedicine (2025): 109136.
[25] AneuriskWeb project website. http://ecm2.mathcs.emory.edu/aneuriskweb. Emory University, Department of Math&CS, 2012.
[26] Rajhi, Wajdi, Zakarya Ahmed, As'ad Alizadeh, Zahraa Abed Hussein, Narinderjit Singh Sawaran Singh, Borhen Louhichi, and Walid Aich. "Predicting hemodynamic complexity in thoracic aortic aneurysms with a POD–LSTM surrogate model." Chinese Journal of Physics 98 (2025): 73-85.
[27] Shi, Z., G. Z. Chen, L. Mao, X. L. Li, C. S. Zhou, S. Xia, Y. X. Zhang, et al. "Machine learning–based prediction of small intracranial aneurysm rupture status using CTA-derived hemodynamics: a multicenter study." American Journal of Neuroradiology 42, no. 4 (2021): 648-654.
[28] Tanioka, Satoru, Fujimaro Ishida, Atsushi Yamamoto, Shigetoshi Shimizu, Hiroshi Sakaida, Mitsuru Toyoda, Nobuhisa Kashiwagi, and Hidenori Suzuki. "Machine learning classification of cerebral aneurysm rupture status with morphologic variables and hemodynamic parameters." Radiology: Artificial Intelligence 2, no. 1 (2020): e190077.

[29] Li, Gaoyang, Xiaorui Song, Haoran Wang, Siwei Liu, Jiayuan Ji, Yuting Guo, Aike Qiao, Youjun Liu, and Xuezheng Wang. "Prediction of cerebral aneurysm hemodynamics with porous-medium models of flow-diverting stents via deep learning." Frontiers in Physiology 12 (2021): 733444.
[30] Roache, Patrick J. "Perspective: a method for uniform reporting of grid refinement studies." (1994): 405-413.
[31] Barzegar Gerdroodbary, Mostafa, and Sajad Salavatidezfouli. "Predictive Surrogate Model of Blood Hemodynamics for Patient-Specific Carotid Artery Stenosis." Journal of the Royal Society Interface (2025).
[32] Ansys, I. "ANSYS® Fluent User's Guide, Release 2020 R2." Canonsburg: ANSYS (2020).
[33] Abdi, Hervé, and Lynne J. Williams. "Principal component analysis." Wiley Interdisciplinary Reviews: Computational Statistics 2, no. 4 (2010): 433-459.
[34] Li, Pengzhi, Yan Pei, and Jianqiang Li. "A comprehensive survey on design and application of autoencoder in deep learning." Applied Soft Computing 138 (2023): 110176.
[35] Chatterjee, A. "An introduction to the proper orthogonal decomposition." Current Science (2000): 808-817.
[36] Lea, Colin, Rene Vidal, Austin Reiter, and Gregory D. Hager. "Temporal convolutional networks: A unified approach to action segmentation." In European Conference on Computer Vision, pp. 47-54. Cham: Springer International Publishing, 2016.